J. Fluid Mech. (2023), *vol*. 968, A12, doi:10.1017/jfm.2023.522

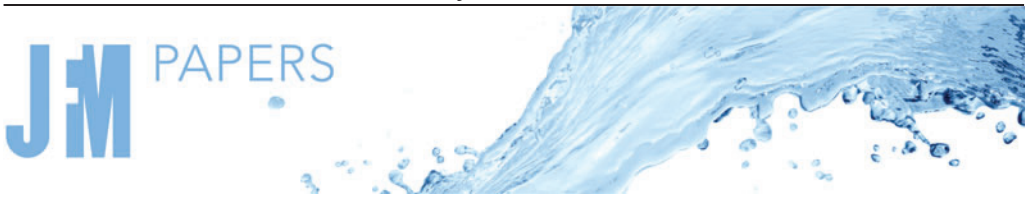

Breaking wave field statistics with a multi-layer model

Jiarong Wu[1], **Stéphane Popinet**[2] **and Luc Deike**[1,3,†]

[1]Mechanical and Aerospace Engineering, Princeton University, Princeton, NJ 08540, USA

[2]Institut Jean Le Rond d'Alembert, CNRS UMR 7190, Sorbonne Université, Paris 75005, France

[3]High Meadows Environmental Institute, Princeton University, Princeton, NJ, 08540, USA

(Received 4 November 2022; revised 10 May 2023; accepted 17 June 2023)

The statistics of breaking wave fields are characterised within a novel multi-layer framework, which generalises the single-layer Saint-Venant system into a multi-layer and non-hydrostatic formulation of the Navier–Stokes equations. We simulate an ensemble of phase-resolved surface wave fields in physical space, where strong nonlinearities, including directional wave breaking and the subsequent highly rotational flow motion, are modelled, without surface overturning. We extract the kinematics of wave breaking by identifying breaking fronts and their speed, for freely evolving wave fields initialised with typical wind wave spectra. The $\Lambda(c)$ distribution, defined as the length of breaking fronts (per unit area) moving with speed c to $c + \mathrm{d}c$ following Phillips (*J. Fluid Mech.*, vol. 156, 1985, pp. 505–531), is reported for a broad range of conditions. We recover the $\Lambda(c) \propto c^{-6}$ scaling without wind forcing for sufficiently steep wave fields. A scaling of $\Lambda(c)$ based solely on the root-mean-square slope and peak wave phase speed is shown to describe the modelled breaking distributions well. The modelled breaking distributions are in good agreement with field measurements and the proposed scaling can be applied successfully to the observational data sets. The present work paves the way for simulations of the turbulent upper ocean directly coupled to a realistic breaking wave dynamics, including Langmuir turbulence, and other sub-mesoscale processes.

Key words: surface gravity waves, wave breaking, air/sea interactions

1. Introduction

Wave breaking occurs at the ocean surface at moderate to high wind speed, with significant impacts on the transfer of momentum, energy and mass between the ocean and the

† Email address for correspondence: ldeike@princeton.edu

atmosphere (Melville 1996; Deike 2022). When waves break, the water surface overturns, which generates sea spray and largely enhances the gas exchange. Visually, it manifests as white capping, widely observable at sea above a certain wind speed. Breaking acts as an energy sink for the waves; it limits the wave height by transferring the excessive wave energy into underwater turbulence and currents, therefore influencing the upper-ocean dynamics as well (McWilliams 2016; Romero, Lenain & Melville 2017).

Describing breaking waves analytically and numerically has been challenging due to their nonlinear nature and the fact that the interface becomes multi-valued. Considering a single breaker, scaling analyses have been successfully proposed for energy dissipation, validated by laboratory experiments (Drazen, Melville & Lenain 2008; Perlin, Choi & Tian 2013); and, thanks to advances in numerical methods and increasing computational power, high fidelity simulations of single three-dimensional (3-D) breakers have emerged (Wang, Yang & Stern 2016; Deike, Melville & Popinet 2016; Gao, Deane & Shen 2021; Di Giorgio, Pirozzoli & Iafrati 2022; Mostert, Popinet & Deike 2022). Other approaches to incorporating breaking wave fields into intermediate-scale modelling include work based on Reynolds averaged Navier Stokes equations and large eddy simulation modelling (Larsen & Fuhrman (2018) and Derakhti *et al.* (2016) among others), but are restricted to individual breaking events or prescribe the breaking statistics instead of resolving it (Sullivan, McWilliams & Melville 2004, 2007).

Phillips (1985) introduced the $\Lambda(\boldsymbol{c_b})$ distribution to describe the statistics of breaking waves, where $\Lambda(\boldsymbol{c_b})\,\mathrm{d}\boldsymbol{c_b}$ is the expected length per unit sea surface area of breaking fronts propagating with speeds in the range of $(\boldsymbol{c_b}, \boldsymbol{c_b} + \mathrm{d}\boldsymbol{c_b})$. The independent variable breaking front propagating speed $\boldsymbol{c_b}$ is chosen in place of wavenumber $\boldsymbol{k}$ because it is a more observable quantity. The link to the wave spectrum is made through the core assumption that c_b is proportional to the wave phase speed c, which in turn relates to k by the linear dispersion relation $c = \sqrt{g/k}$, where g is the gravitational acceleration. The omni-directional $\Lambda(c)$ distribution is predicted to have a c^{-6} shape. The moments of the distribution have a physical interpretation, with the second moment related to the whitecap coverage, the third to mass exchange, the fourth to momentum flux and the fifth to energy dissipation by breaking (Phillips 1985; Kleiss & Melville 2010; Deike & Melville 2018; Romero 2019; Deike 2022).

Several observational studies have been conducted, which provide measurements of the $\Lambda(c)$ distribution, and its moments (Phillips, Posner & Hansen 2001; Melville & Matusov 2002; Gemmrich, Banner & Garrett 2008; Kleiss & Melville 2010; Sutherland & Melville 2013; Banner, Zappa & Gemmrich 2014; Schwendeman & Thomson 2015), made possible by technical advancement including ship-borne and air-borne visible and infrared imagery. Scaling relations have been proposed to describe the breaking statistics for a wide range of conditions, but are facing the usual challenges in the scatter of field data (Sutherland & Melville 2013; Deike & Melville 2018), combined with ongoing discussions about the interpretation of the Phillips (1985) original framework (Banner *et al.* 2014).

Beyond the single breaker description, numerical methods have so far been unable to describe the breaking statistics emerging from an ensemble of propagating surface waves. We propose a numerical framework, leveraging a novel multi-layer formulation of the Navier–Stokes equations and its numerical implementation (Popinet 2020), which is able to capture the multi-scale nonlinear wave field, the intermittent incidences of directional breaking and the highly rotational underwater flow generated by breaking. The wave field is initialised using characteristic wind wave spectra based on field observations. We report the kinematics of the breaking statistics, $\Lambda(c)$, and its scaling with the mean-square slope and discuss how to link our results to field measurements.

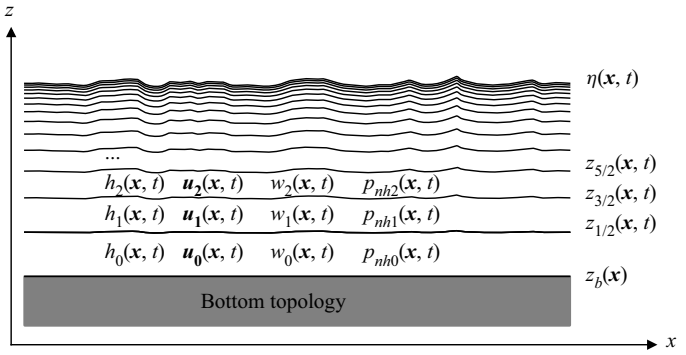

Figure 1. The layers in the multi-layer model, and the fields of each layer. All the fields are functions of horizontal position $\boldsymbol{x} = (x, y)$ and time t. Due to the geometric progression choice, there is a fixed depth ratio between two adjacent layers.

2. Numerical method

2.1. *The multi-layer framework*

We introduce the modelling framework (sketched in figure 1) proposed by Popinet (2020), based on a vertically Lagrangian discretisation of the Navier–Stokes equations. We solve a weak form of the mass and momentum conservation equations in a generalised vertical coordinate. Given N_L layers in total, for layer number l the mass and the momentum conservation equations are (Popinet 2020)

$$\frac{\partial h_l}{\partial t} + \boldsymbol{\nabla}_H \cdot (h\boldsymbol{u})_l = 0, \tag{2.1}$$

$$\frac{\partial (h\boldsymbol{u})_l}{\partial t} + \boldsymbol{\nabla}_H \cdot (h\boldsymbol{u}\boldsymbol{u})_l = -gh_l \boldsymbol{\nabla}_H \eta - \boldsymbol{\nabla}_H (hp_{nh})_l + [p_{nh}\boldsymbol{\nabla}_H z]_l + [\nu \partial_z \boldsymbol{u}]_l, \tag{2.2}$$

$$\frac{\partial (hw)_l}{\partial t} + \boldsymbol{\nabla}_H \cdot (hw\boldsymbol{u})_l = -[p_{nh}]_l + [\nu \partial_z w]_l, \tag{2.3}$$

$$\boldsymbol{\nabla}_H \cdot (h\boldsymbol{u})_l + [w - \boldsymbol{u} \cdot \boldsymbol{\nabla}_H z]_l = 0, \tag{2.4}$$

with l the index of the layer, h its thickness, $\boldsymbol{u}$, w the horizontal and vertical components of the velocity, and p_{nh} the non-hydrostatic pressure (divided by the density). The surface elevation $\eta = z_b + \sum_{l=0}^{N_L} h_l$, and the $[\,]_l$ operator denotes the vertical difference, i.e. $[f]_l = f_{l+1/2} - f_{l-1/2}$. There are five unknowns h_l, $\boldsymbol{u_l}$ (u_{lx}, u_{ly}), w_l and p_{nhl} for each layer. Equation (2.1) represents conservation of volume in each layer for layer thicknesses h_l following material surfaces (i.e. the discretisation is vertically Lagrangian). Equations (2.2) and (2.3) are the horizontal and vertical momentum equations. We only include the vertical diffusion of momentum (i.e. vertical viscosity), with ν the vertical viscosity coefficient, since vertical diffusion is expected to dominate when the horizontal to vertical aspect ratio is large. Note that horizontal diffusion terms can be added when this assumption is not verified. Equation (2.4) is the mass conservation equation. We apply periodic boundary conditions at the left–right, front–back boundaries. The top boundary is a free-slip surface and the bottom is no slip. The time integration includes an 'advection' step and a 'remapping' step. In the 'advection' step, (2.1) to 2.4 are advanced in time. In the 'remapping' step, the layers are remapped, if necessary, onto a prescribed coordinate to prevent any severe distortion of the layer interfaces.

Note that this set of equations does not make any assumption on the slope of the layers, which explains the ∇_{Hz} 'metric' terms appearing in the horizontal momentum equation (2.2) and incompressibility condition (2.4). These metric terms are due to the difference in the slopes of the top and bottom boundaries of the control volumes used to derive the integral conservation equations (see appendix A of Popinet 2020). This is particularly important in the context of steep breaking waves. One can further demonstrate that this set of semi-discrete equations is a consistent discretisation of the incompressible Navier–Stokes equations with a free surface and bottom boundary (Popinet 2020). Note that, in the hydrostatic and small-slope limit, generalised vertical coordinates are widely used in ocean models (Griffies, Adcroft & Hallberg 2020), due to the anisotropic nature of geophysical flows. The choice of the target remapped discretisation is flexible and reflects physical considerations. Here, the remapping step uses a geometric progression of the layer thicknesses which ensures higher vertical resolution of the boundary layer under the free surface.

The numerical schemes (spatial and temporal discretisations, field collocation, grid remapping, etc.) are described in detail in Popinet (2020), and ensure accurate dispersion relations and momentum conservation.

2.2. *Numerical model for breaking*

The dissipation due to breaking is modelled with a simple, *ad hoc* approximation which can be related to the dissipation due to hydraulic jumps in the Saint-Venant system, known to be a surprisingly good first-order model for (shallow-water) breaking waves (Brocchini & Dodd 2008). The horizontal gradient for any layer $\partial z/\partial x$ in (2.2) and (2.4) is limited by a maximum value s_{max}

$$\partial z/\partial x = \begin{cases} \partial z/\partial x, & |\partial z/\partial x| \leqslant s_{max} \\ \mathrm{sign}(\partial z/\partial x) s_{max}, & |\partial z/\partial x| > s_{max}. \end{cases} \tag{2.5}$$

Note that the surface slope $\partial \eta/\partial x$ itself is not affected by this limiter, only the local gradients $\partial z/\partial x$ used in the flux calculation in (2.2) and (2.4). Therefore, the local slope $\partial \eta/\partial x$ can exceed s_{max}.

The maximum local gradient s_{max} is set to 0.577 (30°), and we have verified that the breaking dissipation and kinematics are not sensitive to this choice within a reasonable range (0.4–0.7), both for the single breaking wave cases and the broad-banded wave field cases. In a recent study (McAllister *et al.* 2023), it was found that the local surface slope at breaking onset for a variety of wave spectral bandwidths and shapes approaches a value of 0.5774, which independently supports the use of s_{max} value here. This gradient limiter is sufficient to stabilise the solver, and dissipates some energy. Note that, given enough horizontal resolution and vertical layers, and in the absence of surface overturning, the multi-layer model converges to the Navier–Stokes equations, with underwater turbulence, and the dissipation rate obtained from breaking is close to that obtained with direct numerical simulations. We demonstrate this convergence by a comparison of the multi-layer solver and the two-phase, volume-of-fluid Navier–Stokes solver used in our previous studies (Mostert *et al.* 2022) for a single breaking wave, and show that breaking occurrence and dissipation are not sensitive to the s_{max} parameter.

2.3. *Comparison of the multi-layer and the two-phase Navier–Stokes solvers for a single breaker*

Here, we compare the multi-layer model with a two-phase Navier–Stokes simulation (assumed as 'ground truth') of a single (3-D) breaking wave. We consider a single wave

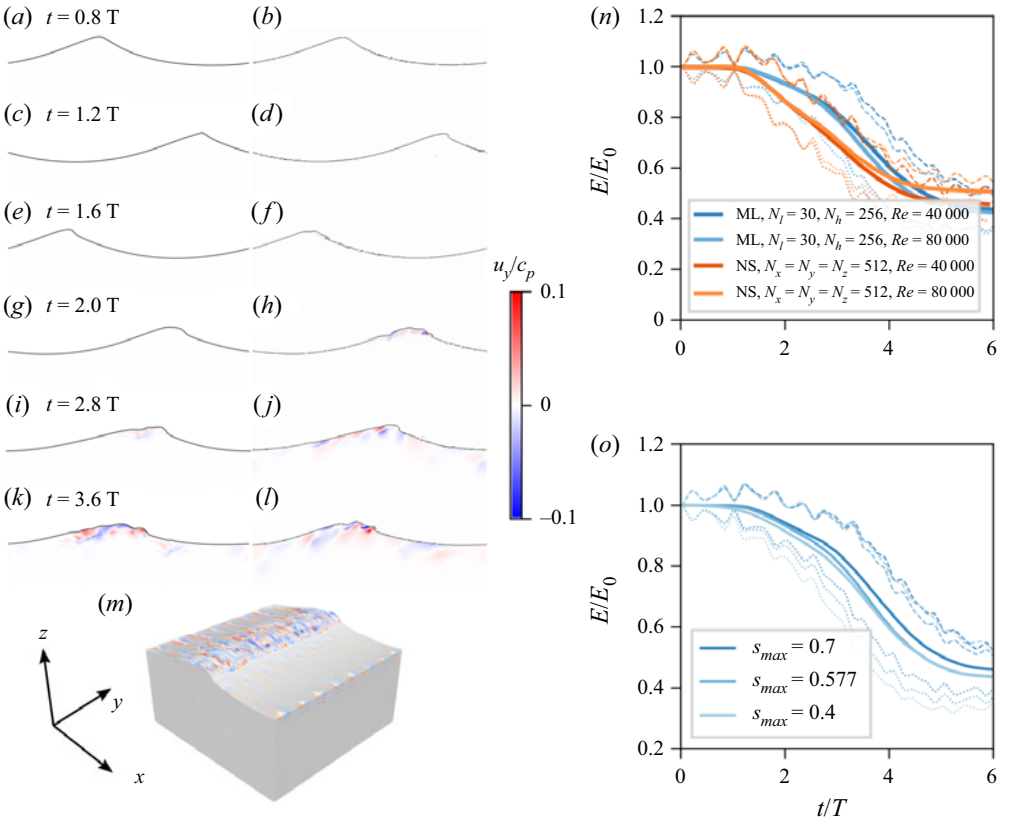

Figure 2. (*a*,*c*,*e*,*g*,*i*,*k*) Snapshots of the wave profile and spanwise velocity u_y on the $y = 0$ central plane slice at times $t = (0.8, 1.2, 1.6, 2.0, 2.8, 3.6)$ T of the multi-layer solver ($256 \times 256 \times 15$ grid); (*b*,*d*,*f*,*h*,*j*,*l*) two-phase Navier–Stokes solver ($256 \times 256 \times 256$ grid) at the same times. (*m*) A 3-D rendering of the single breaking wave case in the multi-layer solver at $t = 3.6$ T. Initial wave steepness $ak = 0.35$, and Reynolds numbers $Re \equiv \sqrt{g\lambda^3}/\nu = 40\,000$, where λ is the wavelength. (*n*) The energy dissipation of the two solvers compared. Dashed line: two times kinetic energy; dotted line: two times potential energy; solid line: total energy. Initial wave steepness $ak = 0.35$. (*o*) The energy dissipation is not sensitive to the specific value of the gradient limiter threshold s_{max}. Initial wave steepness $ak = 0.35$, $Re = 40\,000$.

initialised with a third-order Stokes wave, similar to that in Mostert *et al.* (2022). The two-phase 3-D breaking waves resolved by the two-phase Navier–Stokes solver have been extensively validated against laboratory data in terms of breaking kinematics and energy dissipation due to breaking (Deike *et al.* 2016; Mostert *et al.* 2022).

Figure 2(*a*) plots the underwater spanwise velocity component u_y on the central sliced plane and the travelling wave profiles There is a clear generation of 3-D turbulence once the wave breaks. For the two-phase Navier–Stokes solver, there is surface overturning. The multi-layer solver does not permit surface overturning but the turbulence generation is similar in time and magnitude. Overall, the wave profile of the multi-layer solver closely follows that of the Navier–Stokes solver, and figure 2(*b*) shows that the amount of energy dissipated is close to the Navier–Stokes solver as well. Note that, in Deike *et al.* (2016) and Mostert *et al.* (2022), it has been demonstrated that the energy dissipation in the two-phase Navier–Stokes numerical simulation is in good agreement with laboratory experiments (Rapp & Melville 1990; Drazen *et al.* 2008) of single breaking waves.

We have tested that the energy dissipation is largely independent of the threshold s_{max} in (2.5), as shown in figure 2(*c*) by varying the value of s_{max} between 0.4 and 0.7, which further demonstrates the robustness of the breaking model. Results are also grid converged in terms of the horizontal resolution or number of layers in the multi-layer and grid size in the two-phase solver. In terms of computational time, the multi-layer solver is able to accelerate the calculation by a factor of 40, resulting in approximately 4 CPU hours per wave period integration. The energy dissipation also becomes independent of the Reynolds number at high enough values, as discussed in Mostert *et al.* (2022) (see their figure 3).

3. Statistics of wave breaking

We now analyse the occurrence of breaking fronts as geometric features of the surface height η, while keeping in mind that dissipation as a consequence of breaking is modelled by the *ad hoc* breaking model. We investigate the relation between wave statistics (wave spectrum) and breaking statistics (distribution of length of breaking crest). We demonstrate that the breaking statistics and their relation to the wave statistics can be obtained with the current breaking model and propose a simple scaling relationship.

3.1. *Numerical simulations of actively breaking wave fields*

We initialise the wave field with a directional wavenumber spectrum $F(k, \theta)$. The corresponding azimuth-integrated wavenumber spectrum has the following shape (in agreement with field measurements, see Romero & Melville (2010) and Lenain & Melville (2017); and the discussion in Deike 2022):

$$\phi(k) = Pg^{-1/2}k^{-2.5}\exp[-1.25(k_p/k)^2]. \tag{3.1}$$

The value of P controls how energetic the wave field is, and is of the dimension of velocity, while k_p is the peak wavenumber of the wave spectrum. As shown in § 3.2 and Appendix A, the initial spectral shape will not affect the final analysis in steep enough cases, as the spectra will converge to a shape controlled by the breaking dynamics. The ratio k_pL_0, with L_0 the domain size, is kept constant at a sufficiently large value ($k_pL_0 = 10\pi$) to avoid confinement effects, and we have verified that the results are independent of this ratio. The total water depth is chosen to be $2\pi/k_p$ to ensure a deep-water condition. The directional spectrum is $F(k, \theta) = (\phi(k)/k)\cos^N(\theta)/\int_{-\pi/2}^{\pi/2}\cos^N(\theta)\,\mathrm{d}\theta$, with $\theta \in [-\pi/2, \pi/2]$. The directional spreading is controlled by N, with $N = 5$ for most cases, and we have tested $N = 2$ (more spreading) and $N = 10$ (less spreading).

The initial wave field is a superposition of linear waves: $\eta = \sum_{i,j} a_{ij}\cos(\psi_{ij})$, with the amplitude $a_{ij} = [2F(k_{xi}, k_{yj})\,\mathrm{d}k_x\,\mathrm{d}k_y]^{1/2}$, and the initial random phase $=\psi_{ij} = k_{xi}x + k_{yj}y + \psi_{rand,ij}$. The corresponding orbital velocity is initialised similarly according to the linear wave relation. We use a uniformly spaced initial grid of 32×33 array of (k_{xi}, k_{yj}). The wavenumbers are truncated, and chosen at discrete values of $k_x = ik_p/5$ for $i \in [1, 32]$, and $k_y = jk_p/5$ for $j \in [-16, 16]$, respectively.

That is, the initial wavenumber lower limit is $k_{min}L_0 = 2\pi$ and the upper limit is $k_{trunc}L_0 \approx 225$. The horizontal resolution is $N_x = N_y = 1024$, and layer number $N_L = 15$, with a geometric progression common ratio 1.29. We have verified that the results presented here are numerically converged in terms of layer number, as well as horizontal resolution. We also verified that the results are independent of the box size, i.e. further increasing the ratio of the longest wavelength to the box k_pL_0 does not change the results

discussed here. The current simulation configuration takes approximately 3 h on 64 CPUs to integrate forward 10 peak wave periods, which is computationally very affordable.

3.2. *Evolution of the wave field*

We briefly discuss the transient stage of the wave: i.e. from the initialisation to the point that a quasi-steady spectrum shape is established. The main point is that the stage when the breaking statistics are analysed is independent of the initial spectral shape as long as the initial wave field is steep enough. In breaking-dominated scenarios, we find that approximately $100\omega_p t$ is enough to establish a quasi-steady spectrum independent of the initial shape, and controlled by the steepness of the wave field at that time.

Figure 3(*a*) shows the time evolution of the wave field and the corresponding wave spectrum. Initially steep but smooth superposed linear waves quickly focus and lead to breaking. The focusing and breaking potentially occur via various mechanisms, including both linear and nonlinear focusing. The space–time wave elevation spectrum is shown in figure 3(*b*) and the energy is localised around the curve given by the gravity wave linear dispersion relation $\omega = \sqrt{gk}$, together with an extra branch corresponding to bound waves. Since we start with a truncated spectrum, the initial wave field is smooth while the small-scale features develop over time. There is an energy transfer into the higher wavenumbers which eventually leads to a stable spectrum shape. It is not a Kolmogorov–Zakharov-type wave energy cascade as described by wave-turbulence theory (Zakharov, L'vov & Falkovich 1992), since the weak nonlinearity assumption does not hold and the small features are mostly generated by the breaking events (at a faster rate than weakly nonlinear interaction would act). We verified that the spectrum development is breaking controlled by testing wave spectra that are weakly nonlinear but do not lead to breaking, and then observe a much slower energy transfer into smaller scales over $O(100\omega_p t)$. For the steep enough initial spectra, a quasi-steady spectrum of shape k^{-3} is obtained typically for $\omega_p t > 100$ as shown in figure 3(*c*) with the wave energy spectra independent of the initial spectral shape (demonstrated by comparison with an initial Gaussian spectrum, see Appendix A), and we measure the breaking statistics between $\omega_p t = 124$ and $\omega_p t = 149$.

There are two commonly used measurements of the 'slope' of a broadband wave field: the effective slope $k_p H_s$ and the root-mean-square (r.m.s.) slope σ. The effective slope $k_p H_s$ is essentially a measure of the wave field energy, where the significant wave height $H_s = 4\langle\eta^2\rangle^{1/2}$ is related to the zeroth moment of the spectrum. The r.m.s. slope σ is a measure of how 'rough' the wave field is and is related to the second moment of the spectrum. Here, we define the low-pass filtered steepness parameter $\mu(k)$ as

$$\mu^2(k) = \int_0^k k'^2 \phi(k')\,\mathrm{d}k', \tag{3.2}$$

and σ is the asymptotic value of μ with a cutoff at the highest wavenumber we can numerically resolve k_{max}

$$\sigma^2 = \mu^2(k \to k_{max}). \tag{3.3}$$

The value of $k_{max}L_0$ is set to $2\pi N_h/16$ based on the resolution convergence check (see Appendix B). Here, $N_h = N_x = N_y$ is the horizontal number of grid points and is 1024 for all the results reported. We note that another way of inferring the same quantity is from the variance of the slope distribution (see e.g. Cox & Munk 1954; Munk 2009).

Since there is no forcing mechanism, the total wave energy is slowly decaying (as shown in figure 3*d*). The Reynolds number defined by the peak wavelength λ_p is $Re_p =$

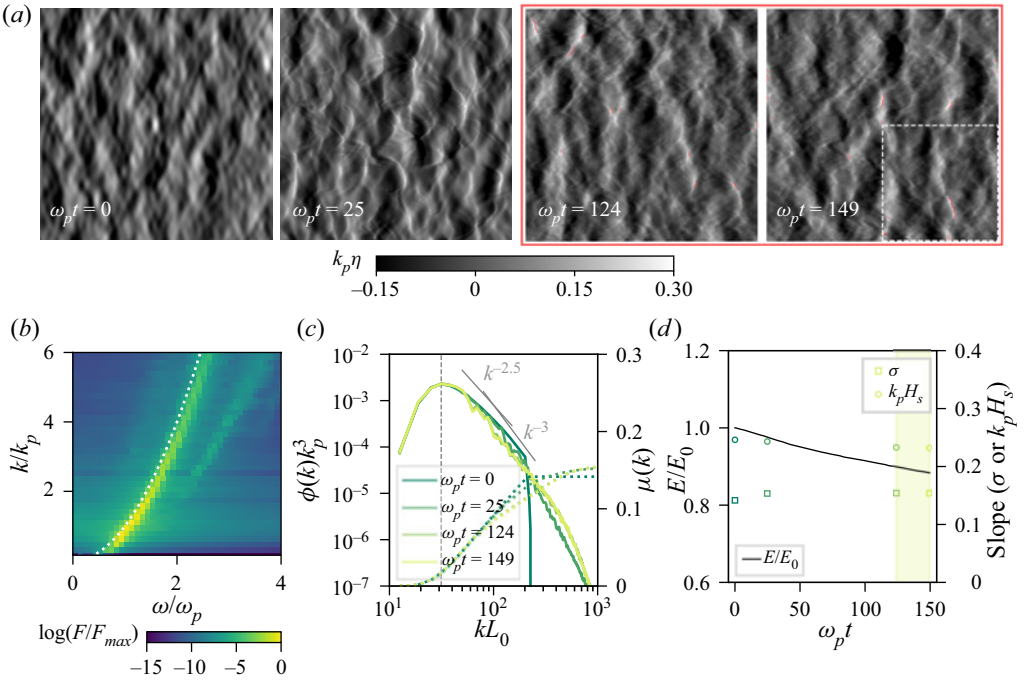

Figure 3. (*a*) Snapshots of the wave field development for the case of root-mean-square (r.m.s.) slope $\sigma = 0.153$. Breaking statistics are collected between $\omega_p t = 124$ and $\omega_p t = 149$ (indicated by the red box). (*b*) The wave energy spectrum on the frequency–wavenumber plane. The dotted white line is the linear dispersion relation of surface gravity waves $k = \omega^2/g$. (*c*) Time evolution of the omni-directional wave spectrum $\phi(k)$, corresponding to the snapshots in (*a*). (*d*) Energy and σ slope evolution of the wave field. Black line: evolution of wave energy (as the sum of potential and kinetic energy integrated over the whole field). Squares: the r.m.s. slope σ of the four snapshots shown in (*a*); circles: the effective slope k_pH_s of the four snapshots shown in (*a*). The breaking statistics are collected during the shaded time interval.

$\lambda_p\sqrt{g\lambda_p}/\nu = 3.17 \times 10^7$, and the dissipation is Reynolds number independent. Instead, the dissipation is primarily due to the numerical gradient-limiter, and is of the order of magnitude of known dissipation due to breaking (Drazen *et al.* 2008; Romero 2019). We have also verified that the spatially and temporally averaged statistics are a good representation of the ensemble average, mainly because the domain size is large enough.

3.3. *Procedure of breaking front detection and velocity measurement*

The wave field evolves and breaking occurs intermittently in space and time. We detect the breaking fronts and their velocity, and construct the length of breaking crest distribution. The breaking fronts are defined geometrically as sharp enough ridges of the surface, as illustrated in figure 4(*a*). Given a surface elevation $\eta(x, y)$ at one time instance, we find its Gaussian curvatures κ_1 and κ_2, and determine the location of the breaking fronts by the threshold $\kappa_2 < -3k_p$ ('ridges' of the η surface), which works well across the different scales. The Gaussian curvatures are computed from the Hessian matrix $H(x, y)$ of surface elevation $\eta(x, y)$. Here, $H(x, y)$ is defined as $H(x, y) = \begin{bmatrix} \eta_{xx} & \eta_{yx} \\ \eta_{xy} & \eta_{yy} \end{bmatrix}$, where η_{xx}, η_{xy}, η_{yy} are the spatial second-order derivatives of η. The Gaussian curvatures κ_1, κ_2 ($|\kappa_1| < |\kappa_2|$) are the eigenvalues of this 2×2 matrix. (Since the matrix is symmetric, the eigenvalues are always real.)

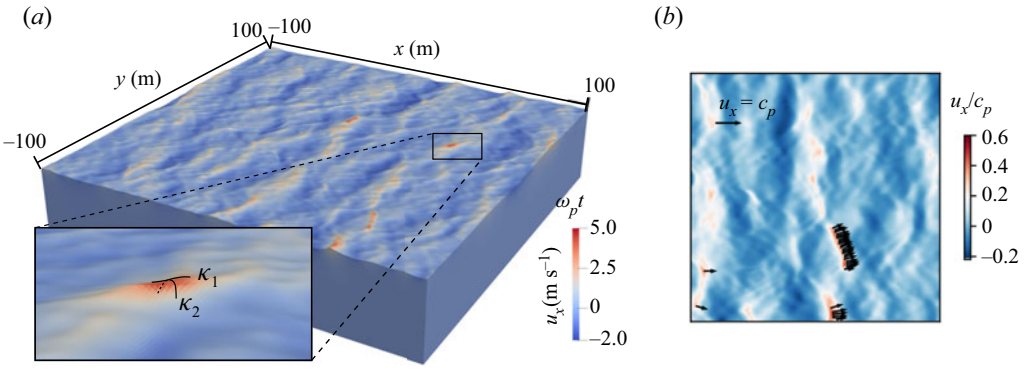

Figure 4. (*a*) A 3-D rendering of the breaking wave field with the colour indicating the surface layer flow velocity. Inset shows the curvature of the breaking fronts as the detection criterion. (*b*) A more focused view taken from the dotted white square in figure 3(*a*). The arrows are showing the velocity magnitude and direction of each length element of the breaking fronts.

After the breaking regions (areas) are detected, we extract the breaking fronts (lines), shown in figure 4(*b*). Then, we use the surface layer Eulerian velocity ($\boldsymbol{u}_{l-1}$ in figure 1) as an estimate of the Lagrangian velocity of the breaking fronts $\boldsymbol{c_b}$. The velocity is mapped on each discretised cell on the lines, which represents an element of length L_0/N_x. Figure 4(*b*) shows the mapped velocity magnitude and direction with arrows. The directionality of $\boldsymbol{c_b}$ is not discussed in this work, i.e. we only consider the magnitude $c_b = |\boldsymbol{c_b}|$. We have tested an alternative velocity mapping method by computing the correlation function between two consecutive images of the detected crests (similar to particle tracking velocimetry), and found no significant difference in the velocity magnitude detected or the resulting $\Lambda(c_b)$ distribution.

We follow Phillips (1985), Kleiss & Melville (2010) and Sutherland & Melville (2013) and assume that $c = c_b$; and we use a correspondence between the breaking front velocity and the underlying wavenumber through the dispersion relation $c = \sqrt{g/k}$. We note that observations have shown that $c_b = \alpha c$, where α is between 0.7 and 0.95 (Rapp & Melville 1990; Banner *et al.* 2014; Romero 2019), at least for large breakers. In the processing we filter out the smaller-scale breakers by imposing a filter $\eta(x, y) > 2.5\langle\eta^2\rangle^{1/2}$. This means that only the large breakers with surface elevation above 2.5 r.m.s. value are included. As a result, no further corrections for the underlying long-wave orbital velocity are needed.

3.4. *The $\Lambda(c)$ distribution of different wave fields*

We study the relation of the breaking statistics to the wave spectra. Figure 5(*a*) shows the (later quasi-steady stage) wave spectra for the various conditions, with variations in spectrum maxima larger than one order of magnitude, and described by power laws ranging from $\phi(k) \propto k^{-2.5}$ to $\phi(k) \propto k^{-3}$. Although the energy near the peak frequency varies, a fixed level of saturation seems to be reached for the steeper cases with overlapping spectra in the k^{-3} range.

As we see in figure 5(*a*), the value of $\mu(k)$ plateaus due to the drop off of the spectrum. In weak nonlinear theories (such as wave-turbulence theory), $\mu < 0.1$ is used to justify the asymptotic expansions, at least for the range of k considered (Zakharov *et al.* 1992). All the breaking cases in our simulation have μ close to or higher than 0.1, underlying the strong nonlinearity of the breaking wave field. The correlation between the two global

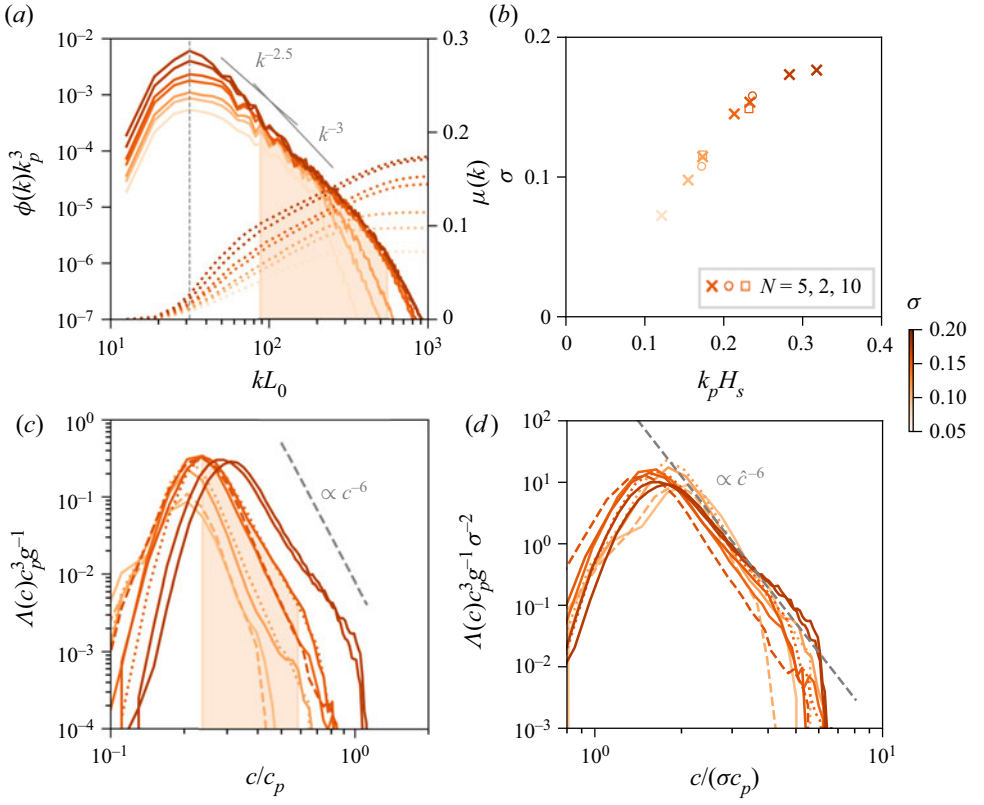

Figure 5. Wave energy spectra of different steepnesses and their $\Lambda(c)$ distribution. The colours correspond to different σ slopes according to the colour bar. (*a*) The wave energy spectra during the breaking statistics collection time interval in non-dimensional form; the vertical grey line is $k_pL_0 = 10\pi$. Darker colour indicates larger global slope k_pH_s (see (*b*) for the values). (*b*) The correlation of r.m.s. slopes σ and the global slopes k_pH_s in the simulated cases. Crosses: $N = 5$; circles: $N = 2$; squares: $N = 10$. (*c*) The non-dimensional breaking distribution $\Lambda(c)$ normalised by c_p and g. Solid lines: directional spreading parameter $N = 5$; dashed lines: $N = 2$; dotted lines: $N = 10$. (*d*) Proposed scaling for the $\Lambda(c)$ distribution using σ and c_p. The pre-factor of the dotted line is 800.

slope parameters k_pH_s (zeroth moment of the spectrum) and σ (second moment of the spectrum) is shown by figure 5(*b*), which we caution is specific to the spectrum shape.

Figure 5(*c*) shows the breaking distribution $\Lambda(c)$ for increasing σ (and k_pH_s) values and the various directionalities. There is no breaking for the smallest $\sigma = 0.0724$ case ($k_pH_s = 0.121$) (not shown in figure 5*c*). An increase in slope to $\sigma = 0.0978$ ($k_pH_s = 0.155$) and $\sigma = 0.114$ ($k_pH_s = 0.173$) starts to generate breakers. The extent of breaking speeds is further increased for the steeper cases with $\sigma > 0.101$, with a clear $\Lambda(c) \propto c^{-6}$ scaling up to around $0.9c_p$. This indicates that there exists a critical value of σ, below which the breaking wave field is not saturated, with the threshold expected to depend on the spectrum shape.

The shaded area in figure 5(*c*) spans the range of the breaker velocity between the peak Λ_{max} and $\Lambda(c) = 0.01\Lambda_{max}$ (for the case of $\sigma = 0.153$), where a power law scaling close to $\Lambda(c) \propto c^{-6}$ can be observed. The same range in the k-space is shaded in figure 5(*a*) as well. The upper limit of $\Lambda(c) = 0.01\Lambda_{max}$ corresponds to a lower limit of $k \approx 4k_p$. Above that velocity, breakers near k_p are very rare. We note that removing the filter of

$\eta(x, y) > 2.5\langle\eta\rangle^{1/2}$ only changes the part of the $\Lambda(c)$ distribution left of the peak, but does not affect the part with c larger than the peak. Similarly, further increasing the horizontal resolution would extend the move up and toward even smaller c, but the presented power law region is unchanged.

The $\Lambda(c)$ distributions from spectra of different directionality N are also shown with different lines (dashed lines indicate more spreading ($N = 2$) and dotted lines less spreading ($N = 10$)). For sufficiently steep cases ($\sigma > 0.101$), there is little difference in the $\Lambda(c)$ distribution between cases with different N, while for intermediate steepness ($\sigma = 0.85$ and 0.101), there is a notable sensitivity to N. For the $N = 10$ cases with more concentrated wave energy, there are overall more breaking events.

3.5. *Wave-slope-based $\Lambda(c)$ scaling*

The current set of numerical experiments with different wave spectra enables us to study the non-dimensional scaling of the breaking front distribution $\Lambda(c)$, which has been a goal for many theoretical studies and observational campaigns. The goal is to predict the $\Lambda(c)$ distribution based on some global quantities of the spectrum, leveraging similarity of the breaking processes and the spectral shape.

The seminal work of Phillips (1985) predicted a purely wind-based scaling $\Lambda(c) \propto u_*^3 g c^{-6}$ through an energy balance argument (u_* being the wind friction velocity). The wave action balance equation $\mathrm{d}[g\phi(k)/\omega]/\mathrm{d}t = S_{nl}(k) + S_{in}(k) + S_{diss}(k)$ involves the following source terms: divergence of the nonlinear energy flux S_{nl}, wind input S_{in} and dissipation due to breaking S_{diss}, written as (Phillips 1985)

$$S_{nl} \propto g k^{-3} B^3(k), \quad S_{in} \propto g k^{-3} \left(\frac{u_*}{c}\right)^2 B(k), \quad \text{and} \quad S_{diss} \propto g k^{-3} f(B(k)), \qquad (3.4a\text{–}c)$$

with the saturation $B(k) = k^3\phi(k)$, and $f(B(k))$ a functional dependence solely on $B(k)$ (assuming that breaking and consequent dissipation 'are the result of local excesses, however these excesses are produced'). The balance between S_{nl} and S_{diss} leads to $f(B) \propto B^3$, and therefore $S_{diss} \propto g k^{-3} B^{-3}$. The breaking front distribution $\Lambda(c)$ is then obtained by writing the equality between dissipation in the k-space and the c-space: $\epsilon(k)\,\mathrm{d}k = \epsilon(c)\,\mathrm{d}c$. The left-hand side is $\epsilon(k)\,\mathrm{d}k = (S_{diss}\omega)\,\mathrm{d}k$; the right-hand side can be related to the fifth moment of $\Lambda(c)$ through a scaling argument $\epsilon(c)\,\mathrm{d}c = b g^{-1} c^5 \Lambda(c)\,\mathrm{d}c$, where b is a non-dimensional breaking parameter (Duncan 1981; Phillips 1985). Substituting a spectral shape of $\phi(k) \propto k^{-5/2}$ into the S_{diss} would then lead to $\Lambda(c) \propto c^{-6}$. Considering the equilibrium range, $S_{nl} \propto S_{in}$ (Phillips 1985), gives $\phi(k) \propto u_* g^{-1/2} k^{-2.5}$, which leads to

$$\Lambda(c) \propto u_*^3 g c^{-6}. \qquad (3.5)$$

This wind-only scaling was, however, not confirmed by observations. To resolve this, later works (Sutherland & Melville 2013; Deike & Melville 2018, etc.) proposed modification of the scaling using a combination of wind speed, wave spectrum peak speed and significant wave height, in the form of

$$\Lambda(c) c_p^3 g^{-1} (c_p/u_*)^{1/2} \propto (c/\sqrt{g H_s})^{-6}, \qquad (3.6)$$

which significantly improved the collapse between data sets. This modification is empirical and is not based on clear physical reasoning.

In our numerical simulations, since we have no wind forcing, the breaking statistics are expected to scale only with the non-dimensional slope σ and spectrum peak

speed c_p. Shown in figure 5(*d*), by rescaling c using $\hat{c} = c/(\sigma c_p)$ and $\Lambda(c)$ using $\hat{\Lambda}(c) = \Lambda(c)c_p^3 g^{-1}\sigma^{-2}$, we are able to collapse the power law region well (for the sufficiently steep cases). The grey dashed line marks the scaling

$$\Lambda(c)c_p^3 g^{-1}\sigma^{-2} \propto \left(c/(\sigma c_p)\right)^{-6}, \tag{3.7}$$

and the corresponding pre-factor is 800. Alternatively, since the r.m.s. slope σ and the effective slope k_pH_s are correlated, a scaling using k_pH_s could be proposed. However, we have found that σ works better than k_pH_s as a scaling parameter for our simulated cases. The reason is likely because σ as a global parameter is weighted favourably towards the larger k part of the spectrum associated with breaking.

We note that, although most of the curves follow a $\Lambda(c) \propto c^{-6}$ scaling, the two largest σ cases exhibit a shallower slope closer to c^{-5}. We observe that these two cases have the k^{-3} region of the energy spectrum extended further near the peak region, i.e. they have higher energy near the peak than the $k^{-2.5}$ 'equilibrium' shape, which results in more large breakers and therefore a shallower $\Lambda(c)$ slope. Similarly, a deficit of energy in the $k^{-2.5}$ 'equilibrium range' may result in a steeper slope of the power law region, which has been observed in some observational cases as well (Zappa *et al.* 2012). It is consistent with the argument in Phillips (1985) that the c^{-6} power law is a result of a choice of $k^{-2.5}$ spectrum shape.

3.6. *Comparison with observations*

We test our σ-based scaling with observational data sets from field campaigns (Kleiss & Melville 2010; Sutherland & Melville 2013; Schwendeman, Thomson & Gemmrich 2014; Deike, Lenain & Melville 2017) where the spectrum information can be retrieved and re-analysed. The results are plotted in figure 6(*a*) and provide strong evidence that the σ-based scaling can be applied to rescale field data, without further need for wind information. The r.m.s. slope σ_{obs} was computed from the observed wave spectra using (3.3), with a cutoff at $k_{max} = 8\ \mathrm{m}^{-1}$, similar to that in the numerical cases. Data from Schwendeman & Thomson (2015) directly report σ_{obs} from the second moment of the wave spectrum (up to 1 Hz, equivalent to $k \approx 4\ \mathrm{m}^{-1}$). Data from Sutherland & Melville (2013) report the wave spectra measured up to $k = 100\ \mathrm{m}^{-1}$ while Kleiss & Melville (2010) have a lower resolution so that we extended the spectra with a k^{-3} tail up to $k = 8\ \mathrm{m}^{-1}$ to compute σ_{obs}. The reason why the Sutherland & Melville (2013) data set extends much further into the small c range is that infrared imaging was used to capture very small breaking features. The main focus should be on the horizontal and vertical positions of the power law region. In general, the agreement of all three data sets within the numerically resolved range of c gives confidence that the proposed σ-based scaling works well.

The agreement with the two data sets shown in figure 6 is a promising sign that the proposed σ-based scaling can provide a concise and physics-based prediction of $\Lambda(c)$ only using information of the wave energy spectra. However, there are a limited number of data sets that report both the wave energy spectra and $\Lambda(c)$, with more data sets being reported using empirical scaling such as (3.6). To compare with more data sets, and more importantly, to help understand the possible reasons behind the success of the empirical scaling, we perform the following re-analysis of the numerical data by inferring the wind forcing from the wave energy spectrum in the simulation.

Since there is no explicit wind forcing in our simulations, the information of wind speed and fetch/duration are encoded in the spectrum. We use the empirical (but very robust) fetch-limited relationships (Toba 1972) that links the non-dimensional wave energy

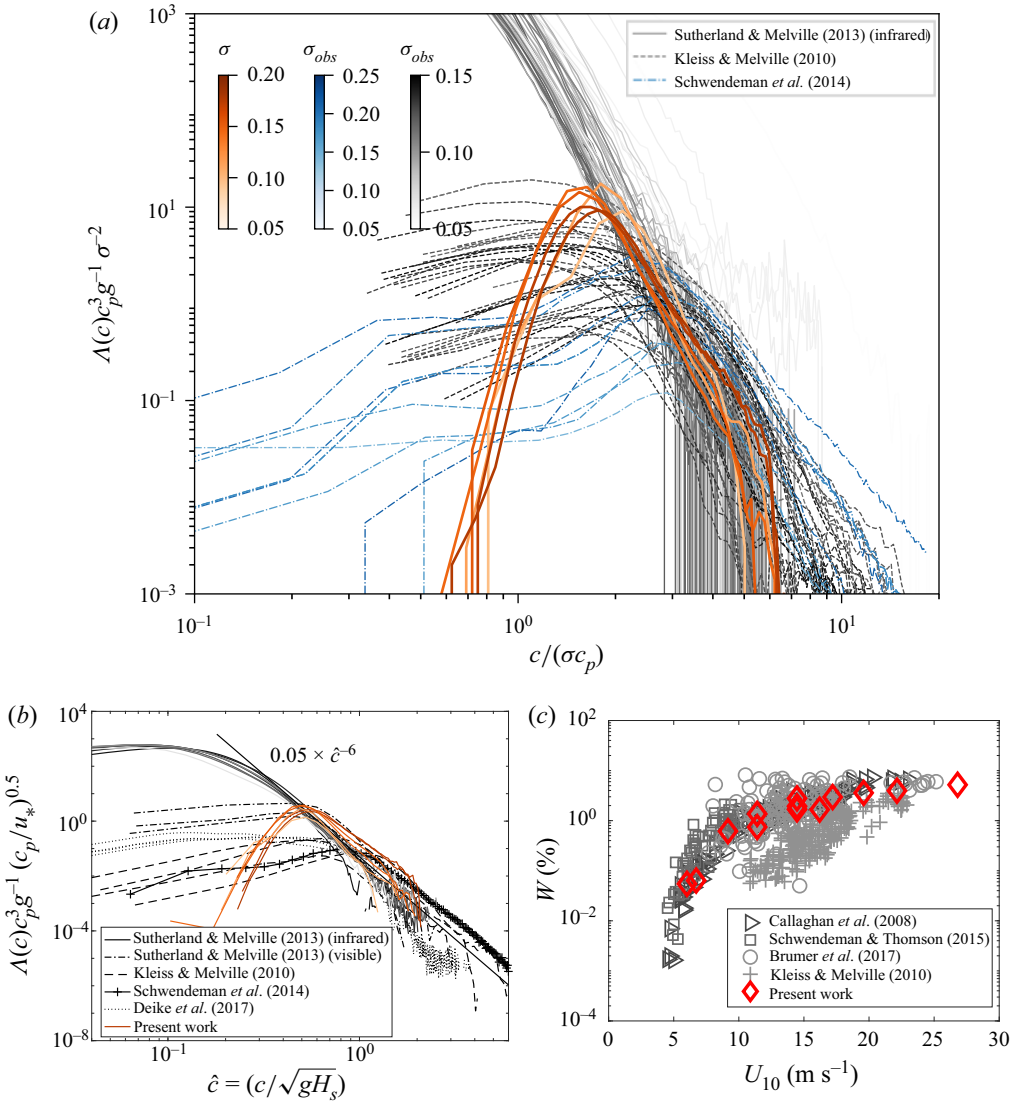

Figure 6. Comparison with observational data. (*a*) Rescaled $\Lambda(c)$ following wave-slope-based scaling proposed by this work. (*b*) Rescaled $\Lambda(c)$ distribution following Sutherland & Melville (2013) with simplifications proposed by Deike (2022). (*c*) Whitecap coverage W as a function of 10 m wind speed U_{10}.

$gH_s u_*^{-2}$ and the non-dimensional frequency $\omega_p g^{-1} u_*$ (wave age u_*/c_p) by

$$gH_s/u_*^2 = C(u_*/c_p)^{-3/2}, \tag{3.8}$$

where C is an order-1 constant. Using (3.8) it is straightforward to show that the scaling equation (3.7) with $\sigma \propto \sqrt{k_p H_s}$ is equivalent to the scaling from Sutherland & Melville (2013), since $k_p H_s \propto (c_p/u_*)^{1/2}$. After that we plot all the data sets using the empirical mixed wind-wave scaling in figure 6(*b*), and good agreement is observed. It indicates that the slope-based scaling is fully compatible with the mixed-wind-slope-based scalings, and the reason for that is the underlying fetch-limited relation. Note that the observational data

are obtained from complex sea states, and do not necessarily have the same spectrum shape as the current numerical data. Some of the observational curves have been bin averaged according to the wave age c/u_* and therefore shows less spreading.

Although we have shown that the proposed slope-based scaling is compatible with the empirical mixed-wind-wave-based one, it provides an alternative form that is both concise and fully interpretable. The wave field at a certain time and space is the result of the wind forcing history, and breaking is caused by excessive energy in the wave spectrum. For a mature and sufficiently steep wave field, breaking (particularly at large scale) is primarily dictated by the wave spectrum itself. Although we do caution that for younger and less steep wave fields, breaking can be more closely coupled to wind forcing. This can be seen from the deviation of curves with very small σ_{obs} in figure 6(*a*), and such conditions require further studies. An additional note is that the original derivation of the $\Lambda(c) \propto c^{-6}$ scaling is based on an energy dissipation argument, whereas in the numerical simulation, breaking is discussed in a purely kinematic sense. It remains to be investigated whether there is a simpler kinematic argument that would give rise to the same $\Lambda(c)$ distribution.

Finally, we can infer classic breaking metrics such as the whitecap coverage from our simulations and compare with more field data sets. The whitecap coverage W quantifies the fraction of the wave surface covered by white foam, and can be estimated through the second moment of $\Lambda(c)$ as $W = 2\pi\gamma g^{-1} \int c^2 \Lambda(c)\,\mathrm{d}c$, where γ is a dimensionless constant representing the ratio of breaking time to wave period (here, $\gamma = 0.56$ following Romero 2019). Figure 6(*b*) shows W as a function of the 10 m wind speed U_{10}; U_{10} is estimated from u_* (inferred using (3.8)) by the COARE parameterisation (Edson *et al.* 2013), which is an empirical relation between u_* and U_{10}. The modelled whitecap coverage falls within the scatter of recent data sets (Callaghan *et al.* 2008; Kleiss & Melville 2010; Schwendeman & Thomson 2015; Brumer *et al.* 2017).

4. Conclusion

We demonstrate that a novel multi-layer model (Popinet 2020) can be used to simulate free-surface waves with strong nonlinearity (and underwater turbulence) with reduced computational complexity compared with a two-phase Navier–Stokes solver. We apply it to study the breaking statistics associated with an ensemble of phase-resolved surface waves simulated in the physical space. We analyse the breaking front distribution introduced by Phillips (1985), and find good agreement with field observations. The breaking distribution largely follows $\Lambda(c) \propto c^{-6}$ even in the absence of wind input, and can be scaled by the wave r.m.s. slope, indicating that the universal breaking kinematics is primarily governed by the wave field itself, while the wind controls the development of the wave spectrum. The proposed scaling in terms of the r.m.s. slope is shown to apply to field data as well.

Our approach provides an unprecedented numerical framework to study breaking statistics for complex wave spectra, which could help to understand the breaking distribution in complex seas (in the presence of swell or currents) and complement existing modelling approaches such as Romero (2019). In addition to the physical discussion of breaking statistics, we demonstrate the capability of the multi-layer approach to solve highly nonlinear geophysical flows with strong vertical–horizontal anisotropy.

Funding. This work was supported by the National Science Foundation (Physical Oceanography) under Grant No. 2122042 to L.D., the High Meadows Environmental Institute Energy and Climate Grand Challenge, the NASA Ocean Vector Winds Science Team 22-OVWST22-0012 and the Cooperative Institute for Earth System Modeling between Princeton and the Geophysical Fluid Dynamics Laboratory (GFDL) NOAA. Computations were partially performed using the Extreme Science and Engineering Discovery Environment (XSEDE), which is supported by NSF Grant No. ACI-1053575; and on resources managed and supported by Princeton

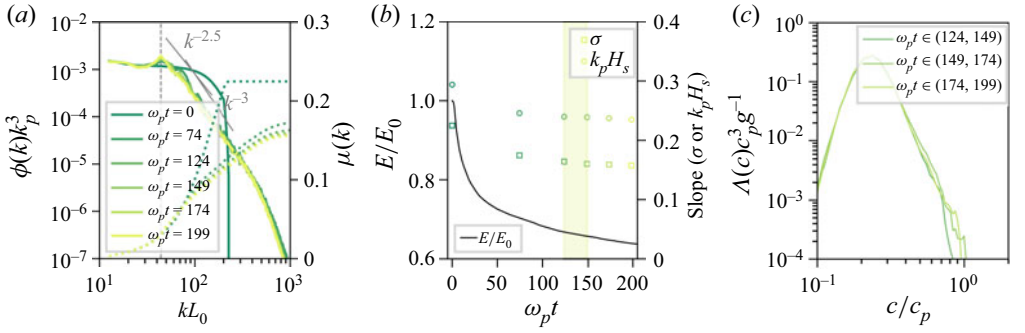

Figure 7. (*a*,*b*) Same as figure 3 but with the initially Gaussian spectra cases. A quasi-steady state spectrum is obtained after $O(100\omega_p t)$, with a k^{-3} shape. (*c*) The $\Lambda(c)$ distribution computed during different time windows in the quasi-steady regime.

Research Computing, a consortium of groups including the Princeton Institute for Computational Science and Engineering and the Office of Information Technology's High Performance Computing Center and Visualization Laboratory at Princeton University. J.W. would also like to acknowledge the support of the Mary and Randall Hack '69 Graduate Award received through the High Meadows Environmental Institute.

Declaration of interests. The authors report no conflict of interest.

Author ORCIDs.
Jiarong Wu https://orcid.org/0000-0003-0637-7952;
Stéphane Popinet https://orcid.org/0000-0001-9947-297X;
Luc Deike https://orcid.org/0000-0002-4644-9909.

Appendix A. Independence of the breaking statistics from the initial spectral shape

In the numerical simulation, we observe that the wave field dissipates the excessive energy and reaches a $\phi(k) \propto k^{-3}$ quasi-steady energy spectrum independent of the initial spectral shape, as long as there is excessive energy initially. This is consistent with the idea of saturation, which dates back to Phillips (1958). It explains that in the limit where the wave field is constrained by breaking, the spectrum should follow a k^{-3} shape. As a result, the breaking statistics are not dependent on the choice of the initial spectral shape either (but still dependent on the steepness).

To demonstrate that the breaking front distribution results are not due to the choice of a particular initial spectral shape, we performed a simulation where the initial spectrum is a Gaussian distribution given by

$$\phi(k) = \frac{P}{s} \exp[-0.5(k - k_p)^2/s^2]. \tag{A1}$$

In addition, we have considered a large variance s of the Gaussian distribution so that there is more energy in the shorter-wave range than a typical wind wave spectrum. We can see from figure 7 that the breaking model quickly dissipates the excessive energy and establishes a quasi-steady k^{-3} distribution. After a quasi-steady spectrum is established, the breaking front distribution exhibits a power law similar to cases initialised with typical wind wave spectra, close to $\Lambda(c) \propto c^{-6}$. In figure 8 we compare the two initial Gaussian spectra cases with the other initial wind wave spectra cases. The correlation between $k_p H_s$ and σ cases is spectrum shape dependent, but the proposed scaling for the $\Lambda(c)$ distribution works as well (because the spectra at late times are independent from the initial conditions) and the pre-factor is the same for all cases.

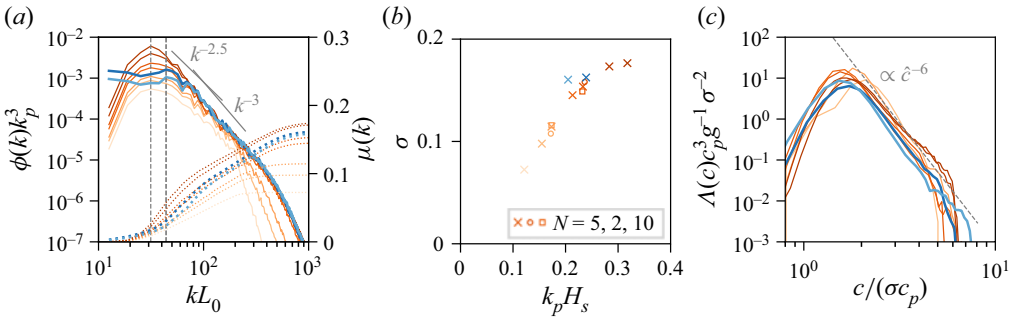

Figure 8. Same as figure 5 comparing the initially Gaussian spectra cases and the wind wave initial spectra. Once a quasi-steady state is reached (due to breaking and loss of excess energy), the wave spectra and breaking distribution are comparable.

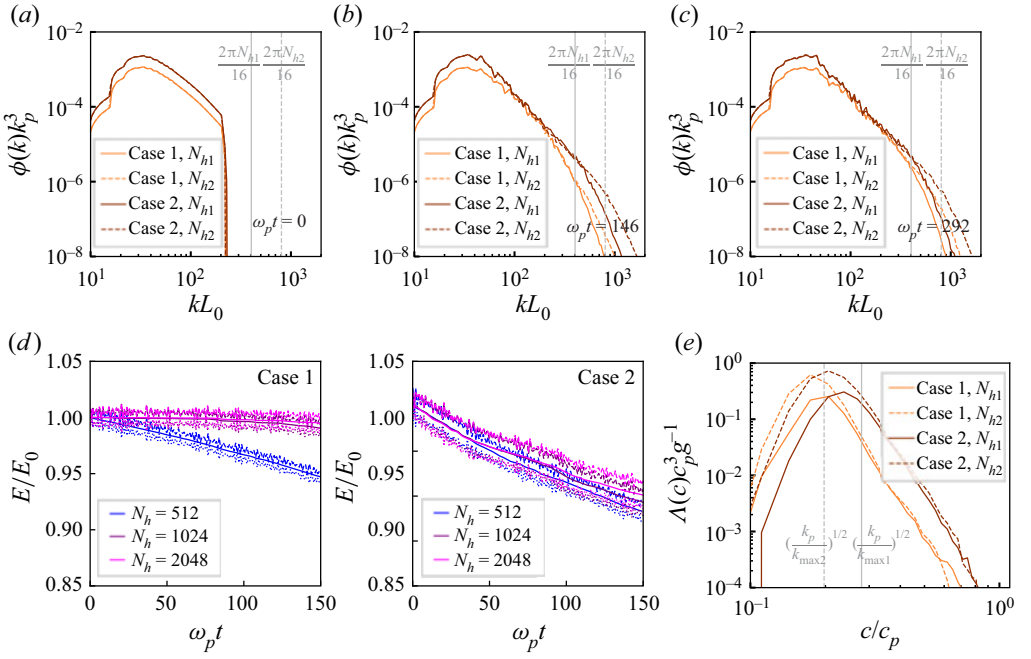

Figure 9. Convergence between horizontal grid point $N_h = 1024$ and 2048. (*a–c*) Wave energy spectra at $\omega_p t = 0$, 146, 292, respectively. The grey vertical lines indicate $k_{max}L_0$ for $N_h = 1024$ and 2048 respectively. (*d*) Energy evolution for case 1 and case 2 with varying horizontal grid points N_h. Solid lines: total energy; dashed lines: two times kinetic energy; dotted lines: two times potential energy. (*e*) Breaking distribution for case 1 and case 2 with varying horizontal grid points N_h. The grey vertical lines indicate the phase speed k_{max} for $N_h = 1024$ and 2048, respectively.

Appendix B. Resolution effects on the wave energy spectrum and breaking statistics

We show with the following verification cases that the wave energy spectra and breaking distributions are converged with respect to the horizontal number of grid point N_h.

Case 1 and case 2 are two cases with different initial energy contents. Their spectrum evolution is shown in figure 9(*a–c*). The spectrum evolution is largely unchanged between horizontal grid point $N_h = 1024$ and 2048 for k smaller than the resolution limit k_{max},

which is determined from 9(*b*,*c*) to be $2\pi/(16\Delta)$, where $\Delta = L_0/N_h$ is the horizontal grid size. We use this value as our upper integration limit k_{max} in σ calculation.

The only discernible change when increasing the resolution is that there is a longer k^{-3} spectral tail in figure 9(*b*,*c*). Apart from the resolution effect, case 1 (less initial energy) has an earlier fall off than case 2 (more initial energy) because of the less frequent breaking events and therefore slower energy transfer to the large k range. In a word, the extent of the k^{-3} range is both breaking limited and resolution limited. Given enough time, case 1 will develop a k^{-3} tail as well.

The energy decay for case 1 and case 2 is shown in figure 9(*d*). Between $N_h = 512$ and 1024 the difference is very significant, especially for the less steep case 1, therefore we use $N_h = 1024$ for all the cases reported in the paper. There remains a small difference in energy dissipation between $N_h = 1024$ and 2048, and the difference is mostly in the kinetic energy, which indicates a discrepancy mostly in the underwater turbulence.

As a result of the convergence in the wave energy spectra, there is a convergence in the breaking distribution $\Lambda(c)$ shown in 9(*e*), for c that are larger than the resolution limit. Again this indicates that the kinematics of breaking is a direct result of the wave energy spectrum, but not strongly coupled to its dynamic effects such as breaking-induced dissipation.

References

Banner, M.L., Zappa, C.J. & Gemmrich, J.R. 2014 A note on the Phillips spectral framework for ocean whitecaps. *J. Phys. Oceanogr.* **44** (7), 1727–1734.

Brocchini, M. & Dodd, N. 2008 Nonlinear shallow water equation modeling for coastal engineering. *ASCE J. Waterway Port Coastal Ocean Engng* **134**, 104–120.

Brumer, S.E., Zappa, C.J., Brooks, I.M., Tamura, H., Brown, S.M., Blomquist, B.W., Fairall, C.W. & Cifuentes-Lorenzen, A. 2017 Whitecap coverage dependence on wind and wave statistics as observed during SO GasEx and HiWinGS. *J. Phys. Oceanogr.* **47** (9), 2211–2235.

Callaghan, A., de Leeuw, G., Cohen, L. & O'Dowd, C.D. 2008 Relationship of oceanic whitecap coverage to wind speed and wind history. *Geophys. Res. Lett.* **35** (23).

Cox, C. & Munk, W. 1954 Statistics of the sea surface derived from sun glitter. *J. Mar. Res.* **13**, 198–227.

Deike, L. 2022 Mass transfer at the ocean–atmosphere interface: the role of wave breaking, droplets, and bubbles. *Annu. Rev. Fluid Mech.* **54** (1), 191–224.

Deike, L., Lenain, L. & Melville, W.K. 2017 Air entrainment by breaking waves. *Geophys. Res. Lett.* **44** (8), 3779–3787.

Deike, L. & Melville, W.K. 2018 Gas transfer by breaking waves. *Geophys. Res. Lett.* **45** (19), 10482–10492.

Deike, L., Melville, W.K. & Popinet, S. 2016 Air entrainment and bubble statistics in breaking waves. *J. Fluid Mech.* **801**, 91–129.

Derakhti, M., Kirby, J.T., Shi, F. & Ma, G. 2016 Wave breaking in the surf zone and deep-water in a non-hydrostatic RANS model. Part 1: organized wave motions. *Ocean Model.* **107**, 125–138.

Di Giorgio, S., Pirozzoli, S. & Iafrati, A. 2022 On coherent vortical structures in wave breaking. *J. Fluid Mech.* **947**, A44.

Drazen, D.A., Melville, W.K. & Lenain, L. 2008 Inertial scaling of dissipation in unsteady breaking waves. *J. Fluid Mech.* **611**, 307–332.

Duncan, J.H. 1981 An experimental investigation of breaking waves produced by a towed hydrofoil. *Proc. R. Soc. Lond.* A **377** (1770), 331–348.

Edson, J.B., Jampana, V., Weller, R.A., Bigorre, S.P., Plueddemann, A.J., Fairall, C.W., Miller, S.D., Mahrt, L., Vickers, D. & Hersbach, H. 2013 On the exchange of momentum over the open ocean. *J. Phys. Oceanogr.* **43** (8), 1589–1610.

Gao, Q., Deane, G.B. & Shen, L. 2021 Bubble production by air filament and cavity breakup in plunging breaking wave crests. *J. Fluid Mech.* **929**, A44.

Gemmrich, J.R., Banner, M.L. & Garrett, C. 2008 Spectrally resolved energy dissipation rate and momentum flux of breaking waves. *J. Phys. Oceanogr.* **38** (6), 1296–1312.

GRIFFIES, S.M., ADCROFT, A. & HALLBERG, R.W. 2020 A primer on the vertical Lagrangian-remap method in ocean models based on finite volume generalized vertical coordinates. *J. Adv. Model. Earth Syst.* **12** (10), e2019MS001954.

KLEISS, J.M. & MELVILLE, W.K. 2010 Observations of wave breaking kinematics in fetch-limited seas. *J. Phys. Oceanogr.* **40** (12), 2575–2604.

LARSEN, B.E. & FUHRMAN, D.R. 2018 On the over-production of turbulence beneath surface waves in Reynolds-averaged Navier–Stokes models. *J. Fluid Mech.* **853**, 419–460.

LENAIN, L. & MELVILLE, W.K. 2017 Measurements of the directional spectrum across the equilibrium saturation ranges of wind-generated surface waves. *J. Phys. Oceanogr.* **47** (8), 2123–2138.

MCALLISTER, M.L., PIZZO, N., DRAYCOTT, S. & VAN DEN BREMER, T.S. 2023 The influence of spectral bandwidth and shape on deep-water wave breaking onset. arXiv:2305.08614.

MCWILLIAMS, J.C. 2016 Submesoscale currents in the ocean. *Proc. R. Soc. Lond.* A **472** (2189), 20160117.

MELVILLE, W.K. 1996 The role of surface-wave breaking in air-sea interaction. *Annu. Rev. Fluid Mech.* **28** (1), 279–321.

MELVILLE, W.K. & MATUSOV, P. 2002 Distribution of breaking waves at the ocean surface. *Nature* **417** (6884), 58–63.

MOSTERT, W., POPINET, S. & DEIKE, L. 2022 High-resolution direct simulation of deep water breaking waves: transition to turbulence, bubbles and droplets production. *J. Fluid Mech.* **942**, A27.

MUNK, W. 2009 An inconvenient sea truth: spread, steepness, and skewness of surface slopes. *Annu. Rev. Mar. Sci.* **1** (1), 377–415.

PERLIN, M., CHOI, W. & TIAN, Z. 2013 Breaking waves in deep and intermediate waters. *Annu. Rev. Fluid Mech.* **45** (1), 115–145.

PHILLIPS, O.M. 1958 The equilibrium range in the spectrum of wind-generated waves. *J. Fluid Mech.* **4** (4), 426–434.

PHILLIPS, O.M. 1985 Spectral and statistical properties of the equilibrium range in wind-generated gravity waves. *J. Fluid Mech.* **156**, 505–531.

PHILLIPS, O.M., POSNER, F.L. & HANSEN, J.P. 2001 High range resolution radar measurements of the speed distribution of breaking events in wind-generated ocean waves: surface impulse and wave energy dissipation rates. *J. Phys. Oceanogr.* **31** (2), 450–460.

POPINET, S. 2020 A vertically-Lagrangian, non-hydrostatic, multilayer model for multiscale free-surface flows. *J. Comput. Phys.* **418**, 109609.

RAPP, R.J. & MELVILLE, W.K. 1990 Laboratory measurements of deep-water breaking waves. *Phil. Trans. R. Soc. Lond.* A **331** (1622), 735–800.

ROMERO, L. 2019 Distribution of surface wave breaking fronts. *Geophys. Res. Lett.* **46** (17–18), 10463–10474.

ROMERO, L., LENAIN, L. & MELVILLE, W.K. 2017 Observations of surface wave–current interaction. *J. Phys. Oceanogr.* **47** (3), 615–632.

ROMERO, L. & MELVILLE, W.K. 2010 Airborne observations of fetch-limited waves in the Gulf of Tehuantepec. *J. Phys. Oceanogr.* **40** (3), 441–465.

SCHWENDEMAN, M. & THOMSON, J. 2015 Observations of whitecap coverage and the relation to wind stress, wave slope, and turbulent dissipation. *J. Geophys. Res.* **120** (12), 8346–8363.

SCHWENDEMAN, M., THOMSON, J. & GEMMRICH, J.R. 2014 Wave breaking dissipation in a young wind sea. *J. Phys. Oceanogr.* **44** (1), 104–127.

SULLIVAN, P.P., MCWILLIAMS, J.C. & MELVILLE, W.K. 2004 The oceanic boundary layer driven by wave breaking with stochastic variability. Part 1. Direct numerical simulations. *J. Fluid Mech.* **507**, 143–174.

SULLIVAN, P.P., MCWILLIAMS, J.C. & MELVILLE, W.K. 2007 Surface gravity wave effects in the oceanic boundary layer: large-eddy simulation with vortex force and stochastic breakers. *J. Fluid Mech.* **593**, 405–452.

SUTHERLAND, P. & MELVILLE, W.K. 2013 Field measurements and scaling of ocean surface wave-breaking statistics. *Geophys. Res. Lett.* **40** (12), 3074–3079.

TOBA, Y. 1972 Local balance in the air-sea boundary processes. *J. Phys. Oceanogr.* **28** (3), 109–120.

WANG, Z., YANG, J. & STERN, F. 2016 High-fidelity simulations of bubble, droplet and spray formation in breaking waves. *J. Fluid Mech.* **792**, 307–327.

ZAKHAROV, V.E., L'VOV, V.S. & FALKOVICH, G. 1992 *Kolmogorov Spectra of Turbulence I*. Springer.

ZAPPA, C.J., BANNER, M.L., SCHULTZ, H., GEMMRICH, J.R., MORISON, R.P., LEBEL, D.A. & DICKEY, T. 2012 An overview of sea state conditions and air-sea fluxes during RaDyO. *J. Geophys. Res.: Oceans* **117** (C7).